**Journal of Pharmaceutical and Medical Research**
**Print ISSN: 2663-1954**
**Online ISSN: 2663-1962**
**DOI: https://doi.org/10.61784/jpmr3086**

# INTEGRATED LIVER TRANSCRIPTOME AND ALTERNATIVE-SPLICING ANALYSIS DEFINES CANDIDATE METABOLIC-INFLAMMATORY AS-DEG REMODELING IN OBSTRUCTIVE JAUNDICE

Abuduwaili Saimaiti
*Emergency and Trauma Center, The First Affiliated Hospital of Xinjiang Medical University, Urumqi 830054, Xinjiang, China.*

**Abstract:** Background: Obstructive jaundice is associated with cholestatic liver injury and intestinal barrier dysfunction, but the hepatic transcriptional and post-transcriptional programs linking these processes remain incompletely defined. Methods: Human intestinal mucosal hematoxylin and eosin staining and qRT-PCR were integrated with liver RNA sequencing from a mouse bile duct ligation (BDL) model. Differentially expressed genes (DEGs), differential alternative-splicing (AS) events, AS-DEG overlap genes, functional enrichment, module activity, RNA-binding/splicing-regulatory factors, and candidate-gene networks were analyzed. Results: BDL induced marked cholestatic liver injury, with increased TBIL, ALT and ALP, and increased plasma diamine oxidase, indicating intestinal barrier-related disturbance. Human intestinal mucosa showed epithelial injury, and qRT-PCR showed significantly higher YWHAG expression and an upward trend of STAT3 in obstructive jaundice samples. RNA-seq of 10 liver samples generated 129.11 Gb clean bases with Q30 values above 97.16%. BDL liver contained 4,718 DEGs and 1,695 differential AS events, with intron retention as the dominant AS type. Integration of expression and splicing identified 340 AS-DEG overlap genes enriched in lipid/xenobiotic metabolism, inflammation and chemotaxis, redox/mitochondrial metabolism, and adhesion/extracellular-matrix remodeling. Ddx28, Rbm3 and Celf4 were upregulated and inversely correlated with the sample-level AS index. Multi-evidence prioritization highlighted Cyp2a22, Ugt1a9, Clcf1, Lifr, Cybb and related candidates. Conclusions: Obstructive jaundice was associated with coordinated hepatic expression and alternative-splicing remodeling that converged on metabolic-inflammatory injury programs and was supported by intestinal mucosal phenotypic evidence. These findings define a hypothesis-generating candidate framework that requires independent isoform-level and functional validation.
**Keywords:** Obstructive jaundice; Bile duct ligation; RNA-seq; Alternative splicing; Intron retention; AS-DEG; Intestinal barrier; Cholestasis

## 1 INTRODUCTION

Obstructive jaundice is a clinically important syndrome caused by impaired bile flow and progressive cholestasis. Beyond biliary obstruction itself, persistent cholestasis can trigger hepatocellular injury, inflammatory activation, metabolic disturbance, and systemic complications that influence perioperative risk and disease progression [1-3]. The liver is therefore not only the primary target organ in obstructive jaundice but also a central site where biliary obstruction is translated into broader metabolic and inflammatory responses.

Intestinal barrier dysfunction is increasingly recognized as an important component of obstructive jaundice. Physiological bile flow helps maintain intestinal mucosal integrity, microbial homeostasis, and luminal defense; when bile flow is interrupted, mucosal injury, increased permeability, bacterial translocation, and endotoxin-related inflammatory responses may occur [4-9]. These observations support a liver-intestine axis in obstructive jaundice. However, most studies have described intestinal injury and hepatic injury as parallel pathological consequences, whereas the molecular programs that connect cholestatic liver damage with intestinal mucosal involvement remain insufficiently resolved.

Transcriptome-wide profiling provides a way to investigate these molecular programs at the systems level. Differential gene-expression analysis can reveal genes and pathways altered during cholestatic injury, including inflammation, lipid metabolism, xenobiotic metabolism, oxidative stress, and tissue remodeling [10-20]. Nevertheless, changes in gene abundance alone cannot fully capture transcriptome remodeling. Alternative splicing is a major post-transcriptional mechanism that expands transcript diversity and reshapes protein isoform usage, and splicing dysregulation has been implicated in inflammatory, metabolic, and liver-related diseases [21-26]. Whether obstructive jaundice induces coordinated changes in hepatic gene expression and alternative splicing, and which genes integrate these two layers of regulation, remains unclear.

The bile duct ligation (BDL) model is widely used to reproduce key features of obstructive cholestatic injury, including bilirubin accumulation, liver injury, inflammation, fibrosis-related remodeling, and systemic effects [27-30]. Because human tissue access is limited and additional mechanistic experiments are not currently available, an integrative bioinformatic strategy can provide a bounded, hypothesis-generating evidence chain by connecting animal-model transcriptomics with human clinical phenotypes. In this context, human intestinal mucosal histology and qRT-PCR

provide clinical support for mucosal involvement, whereas BDL liver RNA-seq is used to identify expression-level and splicing-level molecular alterations that require independent validation.
In the present study, we integrated human intestinal mucosal histopathology and qRT-PCR data with liver RNA-seq from a mouse BDL model to characterize obstructive jaundice-associated transcriptomic and alternative-splicing remodeling. We first confirmed cholestatic liver injury and intestinal barrier-related changes, then profiled differentially expressed genes, differential alternative-splicing events, AS-DEG overlap genes, enriched functional modules, RNA-binding/splicing-regulatory factors, and prioritized candidate genes. This design aimed to define a bioinformatically supported molecular framework linking cholestatic liver injury, intestinal mucosal involvement, metabolic-inflammatory remodeling, and alternative-splicing dysregulation, while recognizing that candidate regulatory relationships require further experimental validation.

## 2 MATERIALS AND METHODS

### 2.1 Study Design

This study was designed as an integrative experimental and bioinformatic analysis to investigate transcriptomic and alternative-splicing alterations associated with obstructive jaundice. The evidence chain consisted of three layers: human intestinal mucosal histopathology and qRT-PCR validation, liver RNA-seq analysis of a mouse bile duct ligation (BDL) model, and multi-layer bioinformatic prioritization of alternative-splicing-related candidate genes. Human histological and qRT-PCR data were used to provide clinical phenotypic and molecular context, whereas the mouse liver RNA-seq dataset was used as the discovery cohort for differential gene expression, alternative splicing, functional enrichment, splicing-factor/RNA-binding protein analysis, and candidate-gene network prioritization.
Human intestinal mucosal specimens were analyzed in an obstructive jaundice group and a control group. For qRT-PCR, 16 human samples were included: B1-B8 were assigned to the control group and A1-A4/A6-A9 were assigned to the obstructive jaundice group. Sample A5 failed RNA quality control and was replaced by the backup sample A9 for downstream qRT-PCR analysis. For histopathological evaluation, representative intestinal mucosal sections from group A and group B were reviewed according to the original pathology report. The tissue name was standardized as intestinal mucosa throughout the manuscript.
For the animal transcriptomic component, 20 specific pathogen-free (SPF) male BALB/c mice aged 8 weeks and weighing 18-20 g were obtained from Cyagen (Suzhou) Biosciences Technology Co., Ltd. After 7 days of adaptive housing, mice were allocated by a random-number table into a sham-operated control group and a BDL model group, with 10 mice in each group. Liver RNA-seq was performed using five sham-operated control samples (control mice 11, 14, 16, 17, and 20; renamed NC_1 to NC_5) and five BDL model samples (model mice 1, 2, 3, 9, and 10; renamed model_1 to model_5).

### 2.2 Mouse BDL Model and Sample Collection

The animal protocol specified 10 BALB/c mice in the control group and 10 BALB/c mice in the model group. Mice were acclimatized for 1 week before surgery. On the day of surgery, mice were anesthetized. Control mice underwent sham surgery with laparotomy only and without bile duct ligation, whereas model-group mice underwent bile duct ligation to induce obstructive jaundice. After surgery, the abdominal cavity was sutured, and mice were maintained under normal feeding conditions after recovery from anesthesia.
On postoperative day 14, serum and plasma were collected from both groups. Serum was used for biochemical detection of alanine aminotransferase (ALT), total bilirubin (TB/TBIL), and alkaline phosphatase (ALP), and plasma was used for ELISA detection of diamine oxidase (DAO). According to the animal protocol, successful model establishment was judged by a significantly higher serum total bilirubin level in the BDL group than in the control group. After euthanasia, liver tissues were photographed in situ and ex vivo, and liver and terminal colon tissues were collected. One portion was fixed in 4% paraformaldehyde for histology, and the remaining portion was snap-frozen in liquid nitrogen for sequencing-related analyses.

### 2.3 Ethics Statement

The animal experimental protocol was reviewed and approved by the Laboratory Animal Welfare and Ethics Committee of Cyagen (Suzhou) Biosciences Technology Co., Ltd. (approval No. TACU23-FY059), and all procedures were performed in accordance with relevant requirements for laboratory animal ethics and welfare.

### 2.4 Histopathological Examination of Human Intestinal Mucosa

Fixed intestinal mucosal tissues were trimmed, dehydrated through graded ethanol, cleared, embedded in paraffin, and sectioned at 4 micrometers. Sections were flattened on a 42 degrees C water bath, mounted onto glass slides, dried at 60 degrees C for 30 min to 1 h, and stored at room temperature before staining.
Hematoxylin and eosin (H&E) staining was performed using hematoxylin (BA-4041; BASO, China) and eosin (BA-4022; BASO, China). The staining workflow included xylene deparaffinization, graded ethanol rehydration, hematoxylin staining, acid alcohol differentiation, eosin staining, dehydration, clearing, mounting, and microscopic examination.

Sections were prepared using a Thermo Fisher Scientific Shandon Finesse 325 microtome, and staining/mounting was performed using a SAKURA Tissue-Tek Prisma Plus system.
Histological evaluation focused on epithelial integrity, mucosal thickness, goblet cell abundance, lamina propria exposure, vascular congestion, edema, inflammatory cell infiltration, ulceration, necrosis, gland loss, connective tissue proliferation, and hemorrhage.

***2.4.1 RNA extraction and quality control for qRT-PCR***

Total RNA was extracted from human tissue samples using a total RNA extraction kit (DP419; TIANGEN, China), according to the service laboratory report. Briefly, 50-100 mg tissue was homogenized in lysis buffer, subjected to phase separation and column purification, and eluted in RNase-free water. RNA concentration and purity were assessed by absorbance at 260/280 nm using a NanoPhotometer N50 spectrophotometer (IMPLEN, Germany). RNA integrity was further evaluated by 1.0% agarose gel electrophoresis.

***2.4.2 qRT-PCR validation***

cDNA synthesis was performed using HiScript III RT SuperMix for qPCR with gDNA wiper (R323-01; Vazyme, China) on a T100 thermal cycler (Bio-Rad, USA). The reverse-transcription program recorded in the report was 42 degrees C for 5 min, 37 degrees C for 15 min, and 85 degrees C for 5 s. qPCR was performed on an ABI QuantStudio 5 system using Hieff qPCR SYBR Green Master Mix (Low Rox Plus; 11202ES03; Yeasen, China). Each 10 microliter qPCR reaction contained 5 microliters SYBR Green Master Mix, 0.5 microliters forward primer (10 micromolar), 0.5 microliters reverse primer (10 micromolar), 2 microliters cDNA, and 2 microliters RNase-free water.
The qPCR cycling program recorded in the instrument program table consisted of pre-denaturation at 95 degrees C for 5 min, followed by 40 cycles of 95 degrees C for 15 s and 60 degrees C for 30 s, with subsequent melt-curve acquisition. Each biological sample was measured in three technical replicates. GAPDH was used as the endogenous reference gene. Relative mRNA expression was calculated using the $2^{-\Delta\Delta Ct}$ method. For manuscript-level statistics, technical replicates were first averaged within each biological sample, and group comparisons were performed between the control group (n = 8) and obstructive jaundice group (n = 8) using Welch's t-test. The qRT-PCR primer sequences were obtained from the service laboratory primer report and are listed in Table 1.

**Table 1** qRT-PCR Primer Sequences Used for Human Intestinal Mucosal Validation

| Gene | Forward primer (5'-3') | Reverse primer (5'-3') |
|---|---|---|
| YWHAG | AGTCTGTGGTCATCGTGGTT | AGGCAAGAAGAGGTGTGAGTAA |
| STAT3 | GCTGTTCTGCCTCACCTGT | GCACTTGTAATGGCGTCTTCA |
| GAPDH | GGTCGGAGTCAACGGATTTG | GGAAGATGGTGATGGGATTTC |

***2.4.3 RNA extraction, library preparation and RNA-seq***

Total RNA for mouse liver RNA-seq was extracted using a total RNA extraction kit (DP419; TIANGEN, China). RNA purity and quantity were assessed by absorbance at 260/280 nm using a NanoPhotometer N50 spectrophotometer (IMPLEN, Germany), and RNA integrity was further assessed using 1.0% agarose gel electrophoresis. Eleven RNA samples were initially extracted and passed quality control; 10 samples were subsequently selected for library construction and sequencing.
RNA-seq library construction was performed by Wuhan Ruixing Biotechnology Co., Ltd. For each selected sample, 1 microgram total RNA was treated with RQ1 DNase (M6101; Promega, USA) to remove genomic DNA. mRNA was captured using VAHTS mRNA capture Beads (N401; Vazyme, China). Strand-specific RNA-seq libraries were prepared using the VAHTS Universal V8 RNA-seq Library Prep Kit for Illumina (NR605; Vazyme, China) and VAHTS RNA Multiplex Oligos Set 1 for Illumina (N323; Vazyme, China). Fragmented RNA was converted into double-stranded cDNA, followed by end repair, A-tailing, adaptor ligation, PCR amplification, purification, quantification, and storage at -80 degrees C before sequencing. The dUTP-marked second cDNA strand was not amplified, enabling strand-specific sequencing. Libraries were sequenced on an Illumina NovaSeq X Plus system using a 150-nt paired-end sequencing mode.
RNA-seq data were evaluated using the clean-read quality-control tables generated by the sequencing pipeline. Clean bases, clean read percentage, Q20, Q30, GC content, duplication rate, and sample correlation were summarized. The 10 RNA-seq samples yielded 129.106 G clean bases in total, and the minimum Q30 value was 97.16%, supporting downstream differential-expression and alternative-splicing analyses. Sample correlation and multidimensional scaling were used to assess group structure and reproducibility.

***2.4.4 Differential gene expression analysis***

Differentially expressed genes (DEGs) between BDL model and control liver samples were obtained from the DESeq output of the original RNA-seq pipeline (model_vs_NC_DESeq). According to the RNA-seq data description document, the default significance criteria for DEG screening were fold change >= 2 or <= 0.5 and adjusted P value < 0.05. The significant DEG table contained gene-level base mean, log2 fold change, standard error, Wald statistic, P value, adjusted P value, sample-level normalized expression values, gene symbol, chromosome, gene type, and gene annotation. In total, 4,718 DEGs were identified, including 3,057 upregulated and 1,661 downregulated genes in the BDL model group.

***2.4.5 Alternative-splicing analysis***

Differential alternative-splicing events were obtained from the original RASE result files for the model_vs_NC comparison. Intron-retention (IR) and non-IR differential splicing files were combined. The source filenames indicated a significance threshold of P < 0.05 and an absolute splicing-ratio difference threshold of 0.15. Alternative-splicing events were summarized by direction, event type, IR/non-IR category, known/novel annotation, gene biotype, and multi-event

genes. A total of 1,695 differential alternative-splicing events were identified, including 674 upregulated and 1,021 downregulated events. Intron retention was the most frequent event type, accounting for 718 events.

#### *2.4.6 Integration of DEGs and alternative-splicing-associated genes*

Alternative-splicing-associated genes were intersected with DEGs using gene identifiers and gene symbols from the original RASG-DEG overlap files. The overlap gene set was used as the main evidence anchor because it linked expression-level dysregulation and transcript-structure alteration within the same genes. In total, 340 genes were identified as both DEGs and alternative-splicing-associated genes. For each overlapping gene, expression direction, log2 fold change, adjusted P value, number of alternative-splicing events, major splicing direction, splicing-event composition, and gene annotation were recorded.

### 2.5 Functional Enrichment and Functional Module Annotation

GO biological process and KEGG pathway enrichment results for the RASG-DEG overlap genes were extracted from the original enrichment output tables. Enrichment terms were ranked using the corrected P value reported by the pipeline, and the top 20 GO biological process and KEGG pathway terms were retained for downstream interpretation. To strengthen the biological logic of the manuscript, enriched terms were further grouped into four functional modules according to term keywords and representative genes: inflammatory immunity and chemotaxis, cell adhesion/extracellular matrix remodeling/angiogenesis, lipid metabolism and drug detoxification, and redox and mitochondrial energy metabolism.

### 2.6 Module Activity Scoring

To evaluate whether functional modules showed coordinated sample-level activity, expression values of RASG-DEG overlap genes within each module were extracted from the DEG table. For each gene, expression values across all RNA-seq samples were standardized to z scores. The module activity score of each sample was then calculated as the mean z score of genes assigned to that module. Modules represented by fewer than three genes were not scored. Module scores were compared between BDL model and control groups using Welch's t-test.

#### *2.6.1 Splicing factor and RNA-binding protein analysis*

To explore potential upstream regulators of the observed alternative-splicing changes, differentially expressed splicing factors and RNA-binding proteins (RBPs) were screened from the DEG table using canonical gene-symbol prefixes associated with splicing regulation and RNA binding, including Srsf, Hnrnp, Rbm, Rbfox, U2af, Sf3, Prpf, Snr, Snrnp, Ddx, Dhx, Tra2, Mbnl, Nova, Ptbp, Qk, Elavl, Celf, Fus, Tardbp, Sfpq, Matr3, Pcbp, Ythdc, Ythdf, and Nono. Candidate splicing factors/RBPs were ranked by adjusted P value.

For each RNA-seq sample, an AS index was calculated as the mean splicing ratio across all differential alternative-splicing events with available sample-level ratio values. Pearson correlation analysis was then performed between splicing factor/RBP expression and the sample-level AS index. This analysis was used to generate regulatory hypotheses and was not interpreted as direct mechanistic validation.

#### *2.6.2 Candidate-gene prioritization and STRING network analysis*

RASG-DEG overlap genes were prioritized using a multi-evidence scoring strategy. The initial priority score was calculated from DEG statistical significance, expression-change magnitude, and alternative-splicing event burden: -log10(adjusted P value) + 2 x absolute log2 fold change + log(1 + number of AS events). A final evidence score was then calculated by adding additional weights for AS event count and functional-module support: priority score + 2 x number of AS events + 5 x number of assigned functional modules. Genes were ranked by the final evidence score.

To obtain external network support, the top candidate genes were submitted to the STRING database through the STRING API using Mus musculus as the species (NCBI taxonomy ID: 10090) and a required interaction score of 400. Candidate protein-protein interaction edges and node degrees were retained for visualization and interpretation. STRING evidence was treated as public database-derived supportive evidence rather than experimental validation.

### 2.7 Statistical Analysis and Data Visualization

Statistical analyses were performed using R and Python. qRT-PCR biological-replicate comparisons and functional-module comparisons were performed using Welch's t-test. Correlations between splicing factor/RBP expression and the AS index were assessed using Pearson correlation. DEG and enrichment analyses used adjusted P values generated by the original sequencing pipeline. Unless otherwise specified, $P < 0.05$ was considered statistically significant. For qRT-PCR, inferential testing used biological samples as the independent statistical unit after averaging technical replicates within each sample.

## 3 RESULTS

### 3.1 BDL Induced Cholestatic Liver Injury and Increased Plasma DAO in Mice

The BDL model produced a robust cholestatic phenotype and liver injury in mice. Compared with sham-operated mice, BDL mice showed markedly higher serum TBIL (165.60 +/- 63.79 vs 1.23 +/- 0.39; n = 10 per group; Welch's t-test, P =

1.91 x 10^-5), ALT (663.60 +/- 501.80 vs 40.23 +/- 12.66; P = 0.0035), and ALP (899.80 +/- 338.50 vs 162.40 +/- 11.75; P = 7.11 x $10^{\wedge-5}$). The corresponding fold changes were 134.6-fold for TBIL, 16.5-fold for ALT, and 5.54-fold for ALP. Plasma diamine oxidase (DAO), a circulating marker commonly used to reflect intestinal barrier injury, was also increased after BDL (18.63 +/- 3.56 vs 10.48 +/- 2.97; n = 10 per group; Welch's t-test, P = 3.15 x $10^{\wedge-5}$; 1.78-fold). These data established that the animal model combined severe cholestatic liver injury with a measurable systemic signal of intestinal barrier disturbance.

Human intestinal mucosa showed epithelial injury and qRT-PCR supported disease-related transcriptional changes

Histological assessment of human intestinal mucosal specimens showed mucosal injury in obstructive jaundice samples (Figure 1a-b). The affected mucosa displayed epithelial exfoliation, exposure of the lamina propria, reduced goblet cells, vascular congestion, inflammatory cell infiltration, and, in severe samples, ulceration, necrosis, glandular loss, connective-tissue proliferation, and hemorrhage. Although mild edema and inflammation were also observed in a subset of control specimens, relatively preserved mucosal architecture with more uniform mucosal thickness and abundant glands was retained in representative control tissue.

qRT-PCR analysis of human intestinal mucosal samples further supported disease-related transcriptional alteration (Figure 1c). When biological replicates were used as the statistical unit, YWHAG expression was significantly higher in obstructive jaundice than in controls (1.97 +/- 0.49 vs 1.25 +/- 0.21; n = 8 per group; Welch's t-test, P = 0.0038; 1.57-fold). STAT3 also showed an upward trend in obstructive jaundice samples (1.28 +/- 0.49 vs 0.94 +/- 0.32; n = 8 per group; Welch's t-test, P = 0.130; 1.35-fold). Therefore, the human H&E and qRT-PCR data were used as clinical phenotypic and molecular support for intestinal mucosal involvement, rather than as direct validation of liver alternative-splicing events.

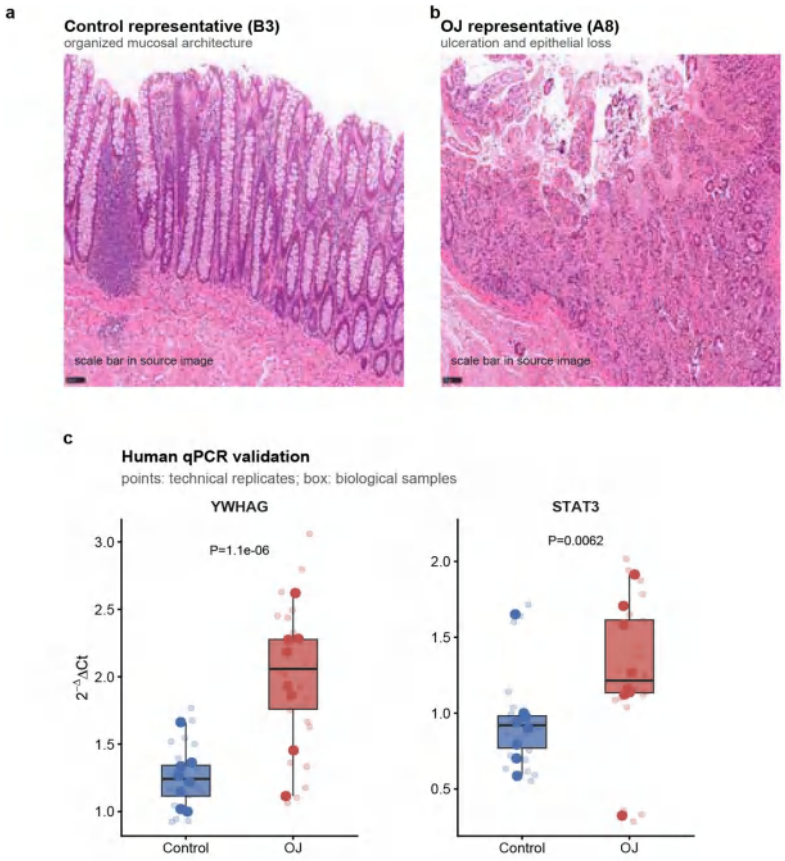


**Figure 1** Human Intestinal Mucosal Injury and qRT-PCR Validation in Obstructive Jaundice

Note: Representative H&E-stained intestinal mucosal sections from control and obstructive jaundice samples, together with qRT-PCR analysis of YWHAG and STAT3 expression. YWHAG was significantly increased in obstructive jaundice samples and STAT3 showed an upward trend, supporting altered mucosal gene expression together with histological injury.

### 3.2 RNA-Seq Data Quality Supported Downstream Transcriptomic and Splicing Analyses

RNA-seq was performed on 10 liver samples, including five sham/control samples and five BDL/model samples (Figure 2a). Across all samples, 129.11 Gb of clean bases were obtained. Sample-level clean bases ranged from 9.27 to 17.52 Gb, the Q30 value was consistently high (minimum 97.16%), and the GC content remained within a narrow range of 48-50% (Figure 2b; Table 2). Clean read percentages ranged from 98.43% to 99.30%. These quality metrics indicated that the dataset was suitable for differential expression and alternative-splicing analyses.

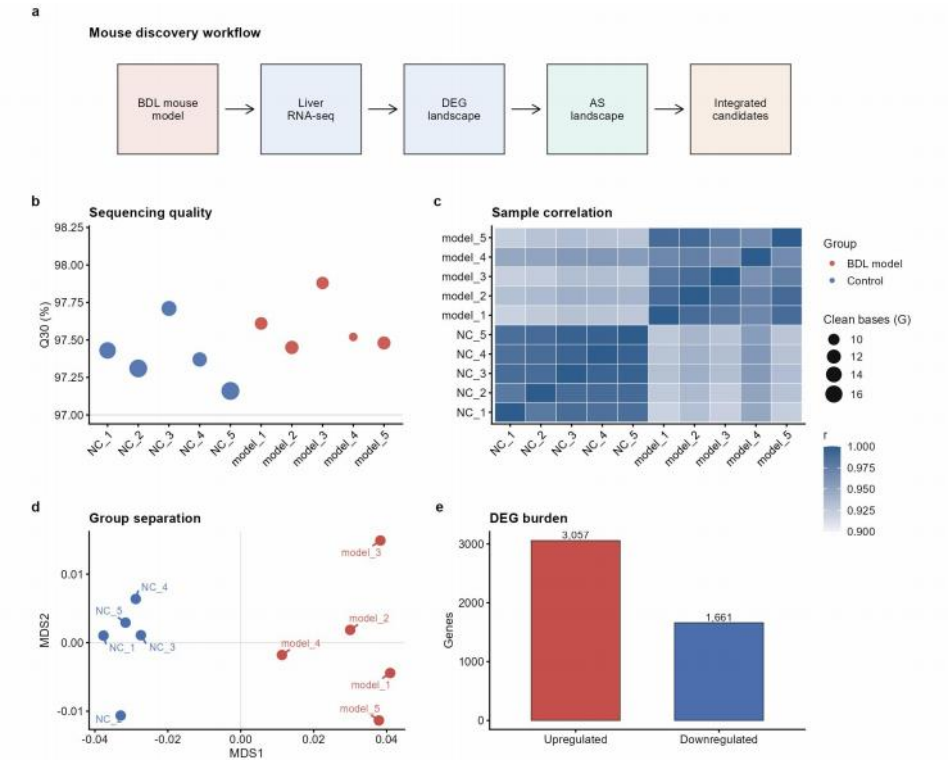


**Figure 2** Mouse Liver RNA-seq Discovery Workflow and DEG Landscape

Note: The figure summarizes the BDL mouse discovery workflow, RNA-seq quality metrics, sample correlation, MDS-based group separation, and the number of upregulated and downregulated DEGs between BDL and control liver samples.

**Table 2** RNA-seq Quality-Control Metrics for Mouse Liver Samples

| Sample | Group | Clean_reads | Clean_bases_G | Q20 | Q30 | GC | Duplicate_rate |
|---|---|---|---|---|---|---|---|
| NC_1 | Control | 110439016 | 15.236 | 99.21 | 97.43 | 49 | 79.28% |
| NC_2 | Control | 123561249 | 17.334 | 99.2 | 97.31 | 48 | 80.49% |
| NC_3 | Control | 93575325 | 13.219 | 99.33 | 97.71 | 48 | 80.20% |
| NC_4 | Control | 88695275 | 12.421 | 99.22 | 97.37 | 48 | 79.23% |
| NC_5 | Control | 125650735 | 17.522 | 99.15 | 97.16 | 48 | 80.81% |
| model_1 | BDL model | 78507694 | 10.842 | 99.33 | 97.61 | 49 | 79.82% |
| model_2 | BDL model | 83013032 | 11.42 | 99.28 | 97.45 | 49 | 79.20% |
| model_3 | BDL model | 77360265 | 10.706 | 99.42 | 97.88 | 50 | 79.50% |
| model_4 | BDL model | 67581709 | 9.27 | 99.31 | 97.52 | 49 | 79.26% |
| model_5 | BDL model | 80979850 | 11.136 | 99.29 | 97.48 | 48 | 77.97% |

### 3.3 BDL Broadly Reshaped the Hepatic Transcriptome

Differential expression analysis identified 4,718 genes that were significantly altered in BDL liver compared with controls using the predefined threshold of fold change >= 2 or <= 0.5 and adjusted P < 0.05 (Figure 2c-d). Among these differentially expressed genes, 3,057 were upregulated and 1,661 were downregulated. This distribution indicated that BDL induced broad transcriptional activation accompanied by suppression of a smaller but substantial set of genes.

### 3.4 BDL Induced Extensive Alternative-Splicing Remodeling Dominated by Intron Retention

A total of 1,695 differential alternative-splicing events were detected in BDL liver (Table 3; Figure 3a). Among these events, 674 were increased and 1,021 were decreased in the model group. Intron retention was the most frequent event type, accounting for 718 events (42.36%), followed by alternative 5' splice-site events (345 events, 20.35%) and alternative 3' splice-site events (217 events, 12.80%). Cassette exon, mutually exclusive exon, exon skipping, and compound splicing patterns accounted for the remaining events (Figure 3b).

Event annotation showed that 1,520 events were associated with protein-coding genes, 158 with lncRNAs, and 16 with pseudogene-related annotations. In addition, 959 events were classified as novel and 736 as known events (Figure 3c). These results indicated that BDL affected both annotated and previously unannotated splicing programs, with intron-retention remodeling representing the dominant feature of the splicing landscape (Figure 3d).

**Table 3** Summary of Differential Alternative-Splicing Events in BDL Liver

| AS_type | Up | Down | Total | Percent |
|---|---|---|---|---|
| IntronR | 256 | 462 | 718 | 42.36 |
| A5SS | 139 | 206 | 345 | 20.35 |

| | | | | |
|---|---|---|---|---|
| A3SS | 73 | 144 | 217 | 12.8 |
| cassetteExon | 57 | 61 | 118 | 6.96 |
| 5pMXE | 50 | 53 | 103 | 6.08 |
| ES | 39 | 29 | 68 | 4.01 |
| 3pMXE | 31 | 35 | 66 | 3.89 |
| A3SS&ES | 10 | 14 | 24 | 1.42 |
| A5SS&ES | 11 | 12 | 23 | 1.36 |
| MXE | 8 | 5 | 13 | 0.77 |

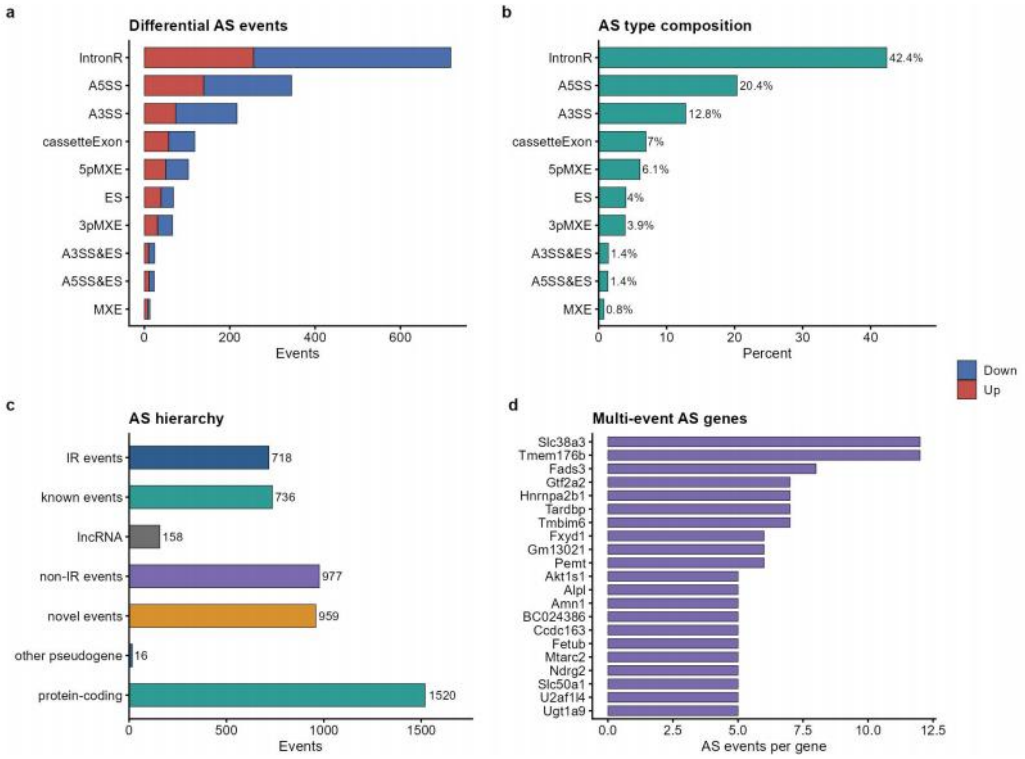


**Figure 3** Alternative-Splicing Landscape in BDL Liver

Note: Distribution of differential alternative-splicing events by direction, event type, intron-retention status, known/novel annotation, and gene biotype. Intron retention represented the dominant event class.

### 3.5 Expression and Splicing Changes Converged on 340 AS-DEG Genes

To identify genes with coordinated transcriptional and post-transcriptional alteration, we intersected genes carrying differential alternative-splicing events with differentially expressed genes. This analysis identified 340 overlapping AS-DEG genes (Figure 4a-b). The overlap provided a focused gene set in which altered expression and altered splicing occurred in the same genes, thereby linking the DEG and AS layers of the BDL response.

### 3.6 AS-DEG Genes were Enriched In Metabolism, Inflammation, Redox Regulation, and Tissue-Remodeling Modules

Functional enrichment analysis of the AS-DEG gene set revealed pathways related to metabolic and inflammatory injury (Figure 4c). The top Gene Ontology terms included oxidation-reduction process (29 input genes; adjusted P = 3.37 x 10^-11), lipid metabolic process (24 genes; adjusted P = 8.23 x 10^-8), xenobiotic metabolic process (9 genes; adjusted P = 1.30 x 10^-6), and steroid metabolic process (10 genes; adjusted P = 4.01 x 10^-6) (Figure 4d). These findings were consistent with disruption of hepatic metabolic and detoxification programs after BDL (Table 4).

**Table 4** Functional Modules Derived from AS-DEG Overlap Genes

| Module | Gene_ count | Control_ mean | BDL_model_ mean | Difference_BDL_ minus_control | Representative_genes |
|---|---|---|---|---|---|
| Adhesion / ECM / angiogenesis | 27 | -0.5514 | 0.5514 | 1.1028 | Cybb, Cd44, Cxcl12, Cxadr, Gpnmb, Gm49368, Myadm, Itga3, Msln, Adam15, Itgb2, Tert, Fes, Cdhr5, Sema3f, Cadm1, Kng1, Csf1r, Pdgfa, Fermt3 |
| Inflammation / chemotaxis | 49 | -0.1838 | 0.1838 | 0.3676 | Clcf1, Lifr, Cybb, Cd44, Il1r1, Cxcl12, Prlr, Prg4, Cd59b, Il1rap, 1810058I24Rik, Jak3, Adam15, Crlf2, Ghr, Tnip2, Pirb, Clu, Itgb2, Igfbp4 |

| | | | | | |
|---|---|---|---|---|---|
| Lipid / xenobiotic metabolism | 50 | 0.5045 | -0.5045 | -1.009 | Hsd11b1, Abhd6, Ugt1a9, Cryl1, Decr2, Ces1d, Acot4, Apol9b, Paox, Gstt2, Cyp46a1, Pm20d1, Acox2, Apol9a, Slc16a11, Upp2, Hint2, Hsd3b3, Rdh16, Abcd3 |
| Redox / mitochondrial energy | 36 | 0.58 | -0.58 | -1.16 | Cyp2a22, Hsd11b1, Cryl1, Cybb, Idh3b, Decr2, Cyp4f14, Mlxipl, Sqor, Cxadr, Paox, Cyp46a1, Uox, Acox2, Hsd3b3, Rdh16, Qdpr, Akr1c13, Sdr9c7, Hsd3b2 |

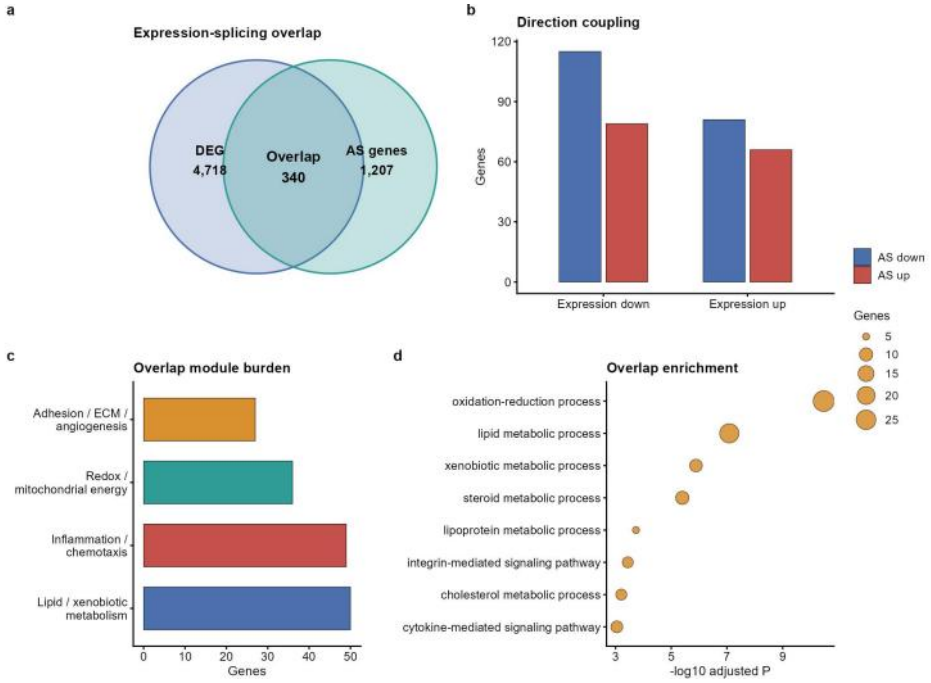


**Figure 4** Integration of Differential Expression and Alternative Splicing

Note: Overlap analysis between DEGs and AS-associated genes identified 340 AS-DEG genes, followed by functional enrichment and module-level interpretation.

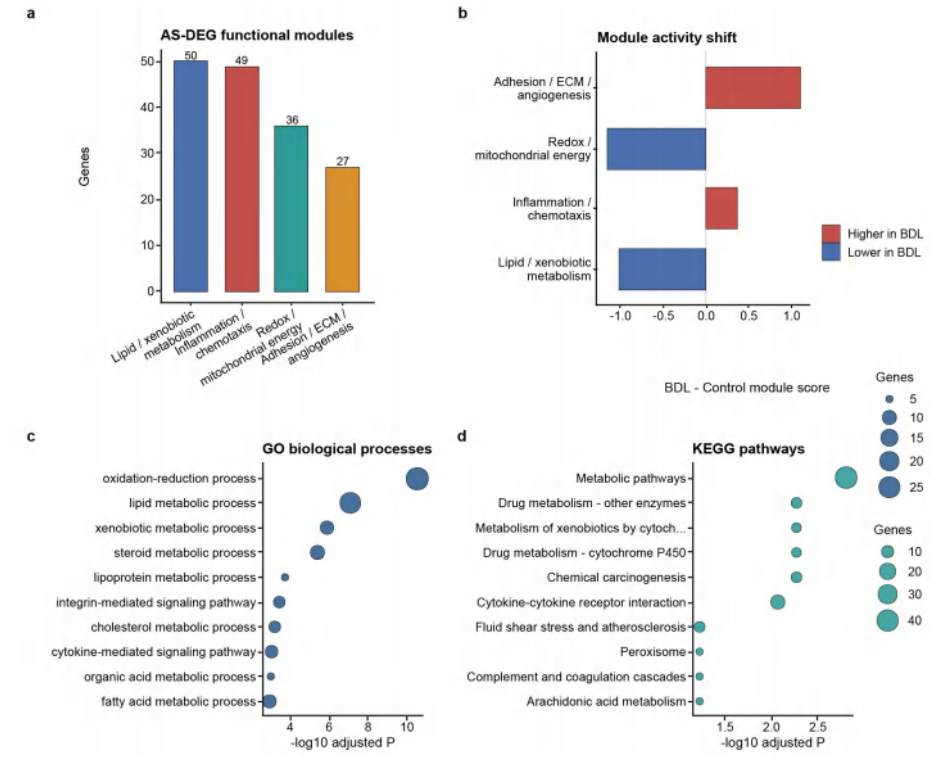


**Figure 5** Functional Modules Associated with AS-DEG Overlap Genes

Note: Functional enrichment and module annotation of genes showing both differential expression and alternative-splicing evidence, highlighting lipid/xenobiotic metabolism, inflammation/chemotaxis, redox/mitochondrial metabolism, and adhesion/extracellular-matrix remodeling.

Module-level annotation further organized the AS-DEG genes into four biologically interpretable processes: lipid and xenobiotic metabolism (50 genes), inflammation and chemotaxis (49 genes), redox and mitochondrial energy metabolism (36 genes), and cell adhesion, extracellular-matrix remodeling, and angiogenesis (27 genes) (Table A1; Figure 5a-b). Representative genes included Abca1, Acox2, Cyp2e1, Cyp46a1, Ugt1a9, and Ces1d in the lipid/xenobiotic module; Cd40, Cd44, Csf1r, Cxcl12, Cybb, and Clcf1 in the inflammation/chemotaxis module; Cyp2a22, Cyp2d10, Decr2, Fmo2, and Hsd11b1 in the redox/mitochondrial module; and Adam15, Col13a1, Itga3, Itgb2, and Gpnmb in the adhesion/remodeling module. Sample-level module scores showed higher activity of the inflammation/remodeling modules and lower activity of metabolic/redox modules in BDL samples, supporting a shift from metabolic homeostasis toward inflammatory tissue remodeling (Figure 5c-d).

### 3.7 Differential RBPs and Splicing Factors were Associated with Sample-Level AS Remodeling

Because large-scale AS remodeling may be linked to altered RNA-binding and splicing-regulatory factors, we examined differentially expressed RBPs/splicing factors. Three regulators, Ddx28, Rbm3, and Celf4, were significantly upregulated in BDL liver (Figure 6a). Ddx28 showed a log2 fold change of 1.38 (adjusted P = 5.50 x $10^{\wedge-16}$), Rbm3 showed a log2 fold change of 1.17 (adjusted P = 1.71 x $10^{\wedge-7}$), and Celf4 showed a log2 fold change of 2.08 (adjusted P = 6.18 x $10^{\wedge-6}$). The global AS index was lower in BDL samples than in control samples, with group means of approximately 0.557 and 0.660, respectively (Figure 6b). Expression levels of the three differentially expressed RBPs/splicing factors were inversely correlated with the sample-level AS index: Ddx28 (r = -0.918, P = 0.00018), Rbm3 (r = -0.868, P = 0.00113), and Celf4 (r = -0.730, P = 0.0166) (Figure 6c, d). These associations are consistent with a relationship between altered splicing-regulatory gene expression and the global AS pattern, but they should be interpreted as hypothesis-generating correlations rather than evidence of direct RBP-mediated splicing control (Table 5).

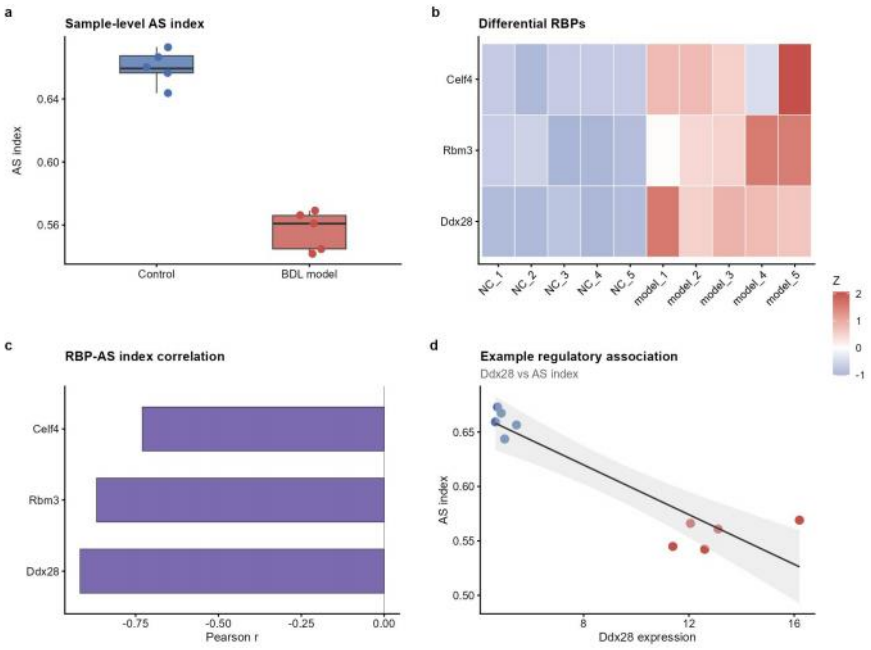


**Figure 6** Differential RBPs/Splicing Factors and Sample-Level AS Index

Note: Expression changes of candidate RNA-binding/splicing-regulatory factors and their correlations with the sample-level AS index. Ddx28, Rbm3 and Celf4 were upregulated and inversely correlated with the AS index.

**Table 5** Differential RNA-binding/Splicing-Regulatory Factors and Correlation with the Sample-Level AS Index

| Symbol | Description | Direction | log2FoldChange | padj | Pearson_r_with_AS_index | Correlation_P |
|---|---|---|---|---|---|---|
| Ddx28 | DEAD box helicase 28 | Upregulated | 1.38130944270596 | 5.503129253187 74e-16 | -0.917639088140376 | 0.000182087516703534 |
| Rbm3 | RNA binding motif (RNP1, RRM) protein 3 | Upregulated | 1.16786417978503 | 1.707503275580 46e-07 | -0.867926790859734 | 0.001131595704726 42 |
| Celf4 | CUGBP, Elav-like family member 4 | Upregulated | 2.0782975996428 | 6.184447254041 85e-06 | -0.729919751905465 | 0.016550058107363 7 |

Multi-evidence prioritization identified candidate genes connecting cholestatic injury, splicing, and functional modules

To prioritize genes most likely to contribute to the BDL-associated transcriptomic phenotype, we integrated differential expression strength, statistical significance, AS-event burden, and functional module annotation (Tables A2-A4; Figure

7a). The highest-ranking candidates included Cyp2a22, Atp10d, Slc13a5, Clcf1, Hsd11b1, Ugt1a9, Abhd6, Lifr, Cybb, Cryl1, Npdc1, and Tmem268. Several of these genes belonged to the major AS-DEG modules, including lipid/xenobiotic metabolism (Ugt1a9, Abhd6, Cryl1), redox and mitochondrial metabolism (Cyp2a22, Hsd11b1, Cybb), inflammation and chemotaxis (Clcf1, Lifr, Cybb), and adhesion/remodeling (Cybb).

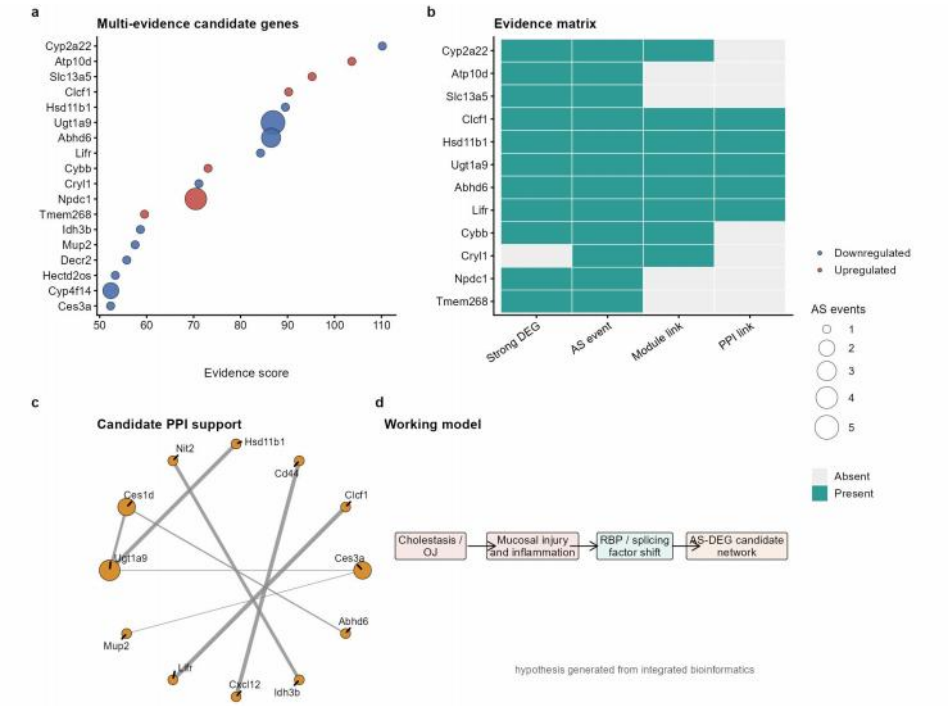


**Figure 7** Multi-Evidence Prioritization and Candidate-Gene Network

Note: Candidate genes were ranked by an integrated evidence score combining DEG significance, expression-change magnitude, AS-event burden, and functional-module support. STRING analysis was used to visualize candidate protein-protein interaction support.

A STRING-based interaction analysis of prioritized candidates identified a connected subnetwork with eight high-confidence interactions (Figure 7b). The strongest interaction pairs included Clcf1-Lifr (interaction score 0.976), Cd44-Cxcl12 (0.932), Hsd11b1-Ugt1a9 (0.917), and Nit2-Idh3b (0.829). Ugt1a9 showed the highest degree within this candidate network, followed by Ces1d and Ces3a (Figure 7c). Together, these results defined a candidate gene set that connects cholestatic liver injury with metabolic disruption, inflammatory remodeling, and alternative-splicing changes (Figure 7d).

## 4 DISCUSSION

This study provides an integrative view of obstructive jaundice-associated liver injury by combining human intestinal mucosal evidence with liver transcriptomic and alternative-splicing analysis in a mouse bile duct ligation (BDL) model. The principal finding is that BDL was accompanied not only by biochemical cholestatic liver injury but also by a coordinated hepatic molecular response involving differential gene expression, broad alternative-splicing (AS) remodeling, functional shifts in metabolic and inflammatory modules, and candidate splicing-regulatory factors. Rather than supporting a single linear mechanism, the current data define a bioinformatically supported framework in which cholestatic injury, intestinal mucosal involvement, metabolic-inflammatory remodeling, and post-transcriptional regulation are linked within the disease process.

The combination of mouse and human evidence strengthens the biological context of the study. In the animal model, marked increases in TBIL, ALT, ALP, and plasma DAO indicated that BDL induced severe cholestatic injury together with a systemic marker related to intestinal barrier disturbance. In human intestinal mucosa, H&E staining showed epithelial damage and inflammatory changes, whereas qRT-PCR showed significant upregulation of YWHAG and an upward trend of STAT3 in obstructive jaundice samples. These findings are consistent with intestinal mucosal involvement in obstructive jaundice and support the liver-intestine axis proposed in the Introduction [4-9]. Importantly, the human data should be interpreted as clinical phenotypic and molecular support, not as direct validation of hepatic AS events detected in the mouse liver.

The DEG and functional-module results indicate that BDL shifted the liver away from metabolic homeostasis and toward inflammatory and tissue-remodeling programs. The downshift of lipid/xenobiotic and redox/mitochondrial modules is biologically plausible in cholestatic injury, where bile-acid accumulation, oxidative stress, and impaired detoxification can interact to reduce metabolic capacity [10-20]. In parallel, the enrichment of inflammation/chemotaxis and adhesion/extracellular-matrix remodeling modules suggests activation of injury-response pathways. This balance between

suppressed hepatic metabolic function and enhanced inflammatory remodeling may help explain why obstructive jaundice often produces systemic effects that extend beyond bile accumulation alone.

A major added layer of this study is the analysis of alternative splicing. BDL induced 1,695 differential AS events, with intron retention representing the dominant event type. Intron retention is often associated with stress responses, transcript surveillance, and altered transcript maturation, and its predominance here suggests that cholestatic injury may perturb RNA processing in addition to changing gene abundance [21-26]. The identification of 340 AS-DEG overlap genes is particularly important because it narrows the analysis to genes altered at both expression and transcript-structure levels. These overlap genes provide a more focused biological anchor than either DEG or AS analysis alone, especially in a study where additional wet-lab mechanistic experiments are not currently available; however, the overlap itself remains an omics-derived prioritization strategy rather than proof of altered protein isoforms or function.

The RBP and splicing-factor analysis further supports the possibility that AS remodeling is not random. Ddx28, Rbm3, and Celf4 were significantly upregulated in BDL liver and inversely correlated with the sample-level AS index. These correlations do not prove that these factors drive the observed splicing events, but they provide a plausible regulatory entry point for future validation. In particular, the inverse association between RBP/splicing-factor expression and the global AS index suggests that the AS landscape may be coupled to a broader stress-regulatory state. This finding should therefore be framed as hypothesis-generating evidence rather than causal mechanism.

The prioritized candidate genes connect the expression, splicing, and functional-enrichment layers into a more interpretable network. Metabolic candidates such as Ugt1a9, Cyp2a22, Hsd11b1, Abhd6, and Cryl1 are consistent with disrupted detoxification, lipid metabolism, and redox balance. Inflammatory and remodeling candidates such as Clcf1, Lifr, Cybb, Cd44, and Cxcl12 point toward cytokine signaling, oxidative inflammatory activity, and cell-adhesion or matrix-related responses. The STRING network further highlighted interaction pairs such as Clcf1-Lifr and Hsd11b1-Ugt1a9, suggesting that the top-ranked candidates may not represent isolated genes but parts of coordinated biological programs. These genes are therefore best viewed as candidate nodes for future mechanistic testing rather than confirmed therapeutic targets.

Several limitations should be acknowledged. First, the human and mouse evidence came from different tissues and species: human data were derived from intestinal mucosa, whereas the discovery transcriptome was generated from mouse liver. The results therefore support a liver-intestine disease framework but do not establish one-to-one cross-species or cross-tissue correspondence. Second, the AS analysis was based on RNA-seq and bioinformatic detection; individual splicing events were not validated by isoform-specific PCR or sequencing. Third, the RBP/splicing-factor and STRING analyses were correlative or database-derived and should not be interpreted as functional proof.

In conclusion, this study suggests that obstructive jaundice is associated with coordinated hepatic transcriptional and post-transcriptional remodeling, with AS-DEG overlap genes converging on metabolic disruption, inflammatory chemotaxis, redox imbalance, and tissue remodeling. The combined evidence supports a working model in which BDL-induced cholestatic injury is accompanied by intestinal mucosal involvement and by hepatic RNA-processing alterations that may shape disease-related molecular programs. Future studies should validate key splicing events and candidate regulators, especially Ugt1a9, Cyp2a22, Clcf1, Lifr, Cybb, Ddx28, Rbm3, and Celf4, in independent samples and functional models.

## COMPETING INTERESTS

The author has no relevant financial or non-financial interests to disclose.

## FUNDING

This work was supported by the Natural Science Foundation of Xinjiang Uygur Autonomous Region (No. 2022D01C225; project title: Mechanistic study of tyrosine 3-monooxygenase/tryptophan 5-monooxygenase activation protein gamma [YWHAG] regulating signal transducer and activator of transcription 3 [STAT3] expression to induce inflammatory responses and promote progression of malignant obstructive jaundice).

## ETHICS APPROVAL AND CONSENT TO PARTICIPATE

The animal experimental protocol was reviewed and approved by the Laboratory Animal Welfare and Ethics Committee of Cyagen (Suzhou) Biosciences Technology Co., Ltd. (approval No. TACU23-FY059). All animal procedures were performed in accordance with relevant requirements for laboratory animal ethics and welfare.

## REFERENCES

[1] Liu JJ, Sun YM, Xu Y, et al. Pathophysiological consequences and treatment strategy of obstructive jaundice. World J Gastrointest Surg, 2023, 15(7): 1262-1276. DOI: 10.4240/wjgs.v15.i7.1262.

[2] Manns MP, Bergquist A, Karlsen TH, et al. Primary sclerosing cholangitis. Nat Rev Dis Primers, 2025, 11(1): 17. DOI: 10.1038/s41572-025-00600-x.

[3] Trivedi PJ, Hirschfield GM, Adams DH, et al. Immunopathogenesis of Primary Biliary Cholangitis, Primary Sclerosing Cholangitis and Autoimmune Hepatitis: Themes and Concepts. Gastroenterology, 2024, 166(6): 995-1019. DOI: 10.1053/j.gastro.2024.01.049.

[4] Sun D, Xie C, Zhao Y, et al. The gut microbiota-bile acid axis in cholestatic liver disease. Mol Med, 2024, 30(1): 104. DOI: 10.1186/s10020-024-00830-x.
[5] Moreno-Gonzalez M, Hampton K, Ruiz P, et al. Regulation of intestinal senescence during cholestatic liver disease modulates barrier function and liver disease progression. JHEP Rep, 2024, 6(10): 101159. DOI: 10.1016/j.jhepr.2024.101159.
[6] Liu M, Ji YL, Hu YJ, et al. Lactococcus garvieae aggravates cholestatic liver disease by increasing intestinal permeability and enhancing bile acid reabsorption. World J Gastroenterol, 2025, 31(10): 101014. DOI: 10.3748/wjg.v31.i10.101014.
[7] Schneider KM, Candels LS, Hov JR, et al. Gut microbiota depletion exacerbates cholestatic liver injury via loss of FXR signalling. Nat Metab, 2021, 3(9): 1228-1241. DOI: 10.1038/s42255-021-00452-1.
[8] Tang B, Tang L, Li S, et al. Gut microbiota alters host bile acid metabolism to contribute to intrahepatic cholestasis of pregnancy. Nat Commun, 2023, 14(1): 1305. DOI: 10.1038/s41467-023-36981-4.
[9] Xia Q, Liu Q, Ma X. Intestinal microbiota in biliary diseases. Curr Opin Gastroenterol, 2023, 39(2): 95-102. DOI: 10.1097/MOG.0000000000000910.
[10] Wu L, Zhou J, Zhou A, et al. Lactobacillus acidophilus ameliorates cholestatic liver injury through inhibiting bile acid synthesis and promoting bile acid excretion. Gut Microbes, 2024, 16(1): 2390176. DOI: 10.1080/19490976.2024.2390176.
[11] Li D, Wan M, Xue L, et al. Zinc promotes microbial p-coumaric acid production that protects against cholestatic liver injury. Cell Host Microbe, 2024, 32(12): 2195-2211.e9. DOI: 10.1016/j.chom.2024.11.002.
[12] Labiano I, Agirre-Lizaso A, Olaizola P, et al. TREM-2 plays a protective role in cholestasis by acting as a negative regulator of inflammation. J Hepatol, 2022, 77(4): 991-1004. DOI: 10.1016/j.jhep.2022.05.044.
[13] Zhuang Y, Ortega-Ribera M, Thevkar Nagesh P, et al. Bile acid-induced IRF3 phosphorylation mediates cell death, inflammatory responses, and fibrosis in cholestasis-induced liver and kidney injury via regulation of ZBP1. Hepatology, 2024, 79(4): 752-767. DOI: 10.1097/HEP.0000000000000611.
[14] Zhang L, Xie P, Li M, et al. Hepatic GDP-fucose transporter SLC35C1 attenuates cholestatic liver injury and inflammation by inducing CEACAM1 N153 fucosylation. Hepatology, 2025, 81(3): 774-790. DOI: 10.1097/HEP.0000000000001003.
[15] Li J, Zhu X, Zhang M, et al. Limb expression 1-like (LIX1L) protein promotes cholestatic liver injury by regulating bile acid metabolism. J Hepatol, 2021, 75(2): 400-413. DOI: 10.1016/j.jhep.2021.02.035.
[16] Zhang L, Pan Q, Zhang L, et al. Runt-related transcription factor-1 ameliorates bile acid-induced hepatic inflammation in cholestasis through JAK/STAT3 signaling. Hepatology, 2023, 77(6): 1866-1881. DOI: 10.1097/HEP.0000000000000041.
[17] Guo Q, Wu Z, Wang K, et al. Forsythiaside-A improved bile-duct-ligation-induced liver fibrosis in mice: The involvement of alleviating mitochondrial damage and ferroptosis in hepatocytes via activating Nrf2. Free Radic Biol Med, 2024, 222: 27-40. DOI: 10.1016/j.freeradbiomed.2024.05.042.
[18] Xie XM, Feng S, Liu T, et al. Role of gut/liver metabolites and gut microbiota in liver fibrosis caused by cholestasis. Int Immunopharmacol, 2024, 139: 112747. DOI: 10.1016/j.intimp.2024.112747.
[19] Song L, Hou Y, Xu D, et al. Hepatic FXR-FGF4 is required for bile acid homeostasis via an FGFR4-LRH-1 signal node under cholestatic stress. Cell Metab, 2025, 37(1): 104-120.e9. DOI: 10.1016/j.cmet.2024.09.008.
[20] Zhang P, Li X, Liang J, et al. Chenodeoxycholic acid modulates cholestatic niche through FXR/Myc/P-selectin axis in liver endothelial cells. Nat Commun, 2025, 16(1): 2093. DOI: 10.1038/s41467-025-57351-2.
[21] Liu Q, Fang L, Wu C. Alternative Splicing and Isoforms: From Mechanisms to Diseases. Genes (Basel), 2022, 13(3). DOI: 10.3390/genes13030401.
[22] Li Y, Xu J, Lu Y, et al. DRAK2 aggravates nonalcoholic fatty liver disease progression through SRSF6-associated RNA alternative splicing. Cell Metab, 2021, 33(10): 2004-2020.e9. DOI: 10.1016/j.cmet.2021.09.008.
[23] Paterson HAB, Yu S, Artigas N, et al. Liver RBFOX2 regulates cholesterol homeostasis via Scarb1 alternative splicing in mice. Nat Metab, 2022, 4(12): 1812-1829. DOI: 10.1038/s42255-022-00681-y.
[24] Rogalska ME, Mancini E, Bonnal S, et al. Transcriptome-wide splicing network reveals specialized regulatory functions of the core spliceosome. Science, 2024, 386(6721): 551-560. DOI: 10.1126/science.adn8105.
[25] Cho S, Chun Y, He L, et al. FAM120A couples SREBP-dependent transcription and splicing of lipogenesis enzymes downstream of mTORC1. Mol Cell, 2023, 83(16): 3010-3026.e8. DOI: 10.1016/j.molcel.2023.07.017.
[26] Webster NJG, Kumar D, Wu P. Dysregulation of RNA splicing in early non-alcoholic fatty liver disease through hepatocellular carcinoma. Sci Rep, 2024, 14(1): 2500. DOI: 10.1038/s41598-024-52237-7.
[27] Weiskirchen R, Weiskirchen S, Tag CG, et al. Induction of Obstructive Cholestasis in Mice. Methods Mol Biol, 2023, 2669: 163-175. DOI: 10.1007/978-1-0716-3207-9_9.
[28] Wu B, Shentu X, Nan H, et al. A spatiotemporal atlas of cholestatic injury and repair in mice. Nat Genet, 2024, 56(5): 938-952. DOI: 10.1038/s41588-024-01687-w.
[29] Jin C, Jiang P, Zhang Z, et al. Single-cell RNA sequencing reveals the pro-inflammatory roles of liver-resident Th1-like cells in primary biliary cholangitis. Nat Commun, 2024, 15(1): 8690. DOI: 10.1038/s41467-024-53104-9.
[30] Awoniyi M, Wang J, Ngo B, et al. Protective and aggressive bacterial subsets and metabolites modify hepatobiliary inflammation and fibrosis in a murine model of PSC. Gut, 2023, 72(4): 671-685. DOI: 10.1136/gutjnl-2021-326500.

**APPENDIX**

**Table A1** Representative GO Biological Process and KEGG Pathway Enrichment Results

| Category | Term | ID | Input_ number | Adjusted_P | Genes |
|---|---|---|---|---|---|
| GO biological process | oxidation-reduction process | GO:0055114 | 29 | 3.37233574399e-11 | Fmo2\|Nos3\|Akr1c13\|Acox2\|Dhrs4\|Uox\|Cyp4f14\|Sdr9c7\|Sqor\|Hsd3b2\|Hsd3b3\|Tm7sf2\|Paox\|Qdpr\|Idh3b\|Cyp46a1\|Cyp2e1\|Cyp2a22\|Decr2\|Cyp4a31\|Hsd11b1\|Cyp2d10\|Gm4756\|Cybb\|Cryl1\|Rdh16\|Sardh\|Acad12\|Cyp2u1 |
| GO biological process | lipid metabolic process | GO:0006629 | 24 | 8.23305430497e-08 | Il1rn\|Sult1b1\|Acox2\|Pla2g6\|Ptgds\|Pm20d1\|Ces1d\|Tm7sf2\|Fads3\|Hmgcs2\|Acnat2\|Hmgcl\|Cyp46a1\|Cyp2e1\|Insig2\|Mogat1\|Decr2\|Hsd11b1\|Rdh16\|Neu2\|Slc16a11\|Acot4\|Abhd6\|Hint2 |
| GO biological process | xenobiotic metabolic process | GO:0006805 | 9 | 1.29776004876e-06 | Fmo2\|Sult1b1\|Cyp2d10\|Akr1c13\|Cyp46a1\|Cyp2e1\|Cyp2a22\|Gsta2\|Cyp2u1 |
| GO biological process | steroid metabolic process | GO:0008202 | 10 | 4.00650929633e-06 | Sult1b1\|Hmgcs2\|Akr1c13\|Dhrs4\|Cyp46a1\|Cyp2e1\|Rdh16\|Insig2\|Hsd11b1\|Tm7sf2 |
| GO biological process | lipoprotein metabolic process | GO:0042157 | 5 | 0.000185270645721 | Apol7a\|Apoc1\|Apol9b\|Apol9a\|Abca1 |
| GO biological process | integrin-mediated signaling pathway | GO:0007229 | 7 | 0.000364291224294 | Fyb\|Gm49368\|Fcer1g\|Itgb2\|Itga3\|Fermt3\|Adam15 |
| GO biological process | cholesterol metabolic process | GO:0008203 | 7 | 0.000623180416306 | Hmgcs2\|Cyp46a1\|Tm7sf2\|Apoc1\|Insig2\|Abca1\|Ces1d |
| GO biological process | cytokine-mediated signaling pathway | GO:0019221 | 8 | 0.000901945783736 | Ghr\|Prlr\|Cd44\|Csf1r\|Pirb\|Lifr\|Il1rap\|Il1r1 |
| GO biological process | organic acid metabolic process | GO:0006082 | 5 | 0.000991683971616 | Fmo2\|Cyp2a22\|Cyp2d10\|Cyp2u1\|Cyp2e1 |
| GO biological process | fatty acid metabolic process | GO:0006631 | 9 | 0.00115775923249 | Cryl1\|Acnat2\|Cyp2e1\|Acox2\|Ptgds\|Decr2\|Fads3\|Pm20d1\|Acot4 |
| KEGG pathway | Metabolic pathways | mmu01100 | 45 | 0.00156326275261 | Nos3\|Ugt1a10\|Acox2\|Auh\|Dhrs4\|Uox\|Gstp2\|Pla2g6\|Sqor\|Hsd3b2\|Gpt\|Ptgds\|Aco2\|Tm7sf2\|Cryl1\|Qdpr\|Prodh2\|Hagh\|Mocs1\|Sardh\|Hykk\|Nit2\|Hmgcs2\|Idh3b\|Gstt2\|Hmgcl\|Hyi\|Cyp2e1\|Pde6c\|Ggt6\|Cyp4f14\|Cyp4a31\|Kyat3\|Hsd11b1\|Upp2\|Alas1\|Pfkfb2\|Car7\|Gsta2\|Atp6v0a4\|Rdh16\|Khk\|Ugt1a9\|Acot4\|Cyp2u1 |
| KEGG pathway | Drug metabolism - other enzymes | mmu00983 | 8 | 0.00538732357019 | Upp2\|Gstt2\|Ugt1a10\|Gsta2\|Gstp2\|Cyp2e1\|Ces1d\|Ugt1a9 |
| KEGG pathway | Metabolism of xenobiotics by cytochrome P450 | mmu00980 | 7 | 0.00538732357019 | Gstt2\|Ugt1a10\|Gsta2\|Gstp2\|Cyp2e1\|Ugt1a9\|Hsd11b1 |
| KEGG pathway | Drug metabolism - cytochrome P450 | mmu00982 | 7 | 0.00538732357019 | Fmo2\|Gstt2\|Ugt1a10\|Gsta2\|Gstp2\|Cyp2e1\|Ugt1a9 |
| KEGG pathway | Chemical carcinogenesis | mmu05204 | 8 | 0.00538732357019 | Gstt2\|Ugt1a10\|Gsta2\|Gstp2\|Cyp2e1\|Ugt1a9\|Kyat3\|Hsd11b1 |
| KEGG pathway | Cytokine-cytokine receptor interaction | mmu04060 | 14 | 0.00855504040158 | Il1rn\|Tgfb3\|Crlf2\|Ghr\|Prlr\|Csf1r\|Cd40\|Il18r1\|Clcf1\|Lifr\|Il1rap\|Cxcl12\|Il15ra\|Il1r1 |
| KEGG pathway | Fluid shear stress and atherosclerosis | mmu05418 | 8 | 0.0594959455343 | Pdgfa\|Nos3\|Rac3\|Gsta2\|Gstp2\|Ikbkg\|Il1r1\|Gstt2 |
| KEGG pathway | Peroxisome | mmu04146 | 6 | 0.0594959455343 | Hmgcl\|Dhrs4\|Acox2\|Paox\|Decr2\|Abcd3 |
| KEGG pathway | Complement and coagulation cascades | mmu04610 | 6 | 0.0594959455343 | Itgb2\|Cfh\|Cd59b\|Kng1\|Clu\|Proc |
| KEGG pathway | Arachidonic acid metabolism | mmu00590 | 6 | 0.0594959455343 | Cyp2e1\|Pla2g6\|Cyp4f14\|Ptgds\|Cyp4a31\|Cyp2u1 |

**Table A2** Prioritized AS-DEG Candidate Genes and Multi-Evidence Scores

| Symbol | Description | Direction | log2FC | padj | AS_event_count | AS_direction_major | AS_type_detail | Module | Evidence_score | Evidence_chain |
|---|---|---|---|---|---|---|---|---|---|---|
| Cyp2a22 | cytochrome P450, family 2, subfamily a, polypeptide 22 | Downregulated | -7.625 | 5.88877590425682e-88 | 1 | down | A5SS:1 | Redox / mitochondrial energy | 110.172 | significant DEG evidence + AS event evidence + redox and mitochondrial energy metabolism + candidate prioritization score |
| Atp10d | ATPase, class V, type 10D | Upregulated | 3.062 | 1.37134949809646e-95 | 1 | up | IntronR:1 | Other | 103.68 | significant DEG evidence + AS event evidence + unclassified + candidate prioritization score |
| Slc13a5 | solute carrier family 13 (sodium-dependent citrate transporter), member 5 | Upregulated | 3.297 | 1.15874458869971e-86 | 1 | down | IntronR:1 | Other | 95.224 | significant DEG evidence + AS event evidence + unclassified + candidate prioritization score |
| Clcf1 | cardiotrophin-like cytokine factor 1 | Upregulated | 4.093 | 4.5006731298542e-75 | 1 | down | IntronR:1 | Inflammation / chemotaxis | 90.226 | significant DEG evidence + AS event evidence + inflammatory immunity and chemotaxis + candidate prioritization score |
| Hsd11b1 | hydroxysteroid 11-beta dehydrogenase 1 | Downregulated | -2.775 | 5.14859105724294e-72 | 1 | up | A3SS:1 | redox and mitochondrial energy metabolism; lipid metabolism and xenobiotic detoxification | 89.532 | significant DEG evidence + AS event evidence + redox and mitochondrial energy metabolism; lipid metabolism and xenobiotic detoxification + candidate prioritization score |
| Ugt1a9 | UDP glucuronosyltransferase 1 family, polypeptide A9 | Downregulated | -4.687 | 1.87483081909176e-61 | 5 | up | A5SS:5 | Lipid / xenobiotic metabolism | 86.893 | significant DEG evidence + AS event evidence + lipid metabolism and xenobiotic detoxification + candidate prioritization score |
| Abhd6 | abhydrolase domain containing 6 | Downregulated | -2.65 | 1.59185446154356e-69 | 3 | down | A5SS:3 | Lipid / xenobiotic metabolism | 86.485 | significant DEG evidence + AS event evidence + lipid metabolism and xenobiotic detoxification + candidate prioritization score |
| Lifr | LIF receptor alpha | Downregulated | -2.73 | 8.31067057240952e-72 | 1 | down | A5SS:1 | Inflammation / chemotaxis | 84.233 | significant DEG evidence + AS event evidence + inflammatory immunity and chemotaxis + candidate prioritization score |
| Cybb | cytochrome b-245, beta polypeptide | Upregulated | 3.543 | 5.17614975844233e-49 | 1 | down | IntronR:1 | redox and mitochondrial energy metabolism; inflammatory immunity and chemotaxis; cell adhesion, matrix remodeling and angiogenesis | 73.065 | significant DEG evidence + AS event evidence + redox and mitochondrial energy metabolism; inflammatory immunity and chemotaxis; cell adhesion, matrix remodeling and angiogenesis + candidate prioritization score |

**Table A3** Prioritized AS-DEG Candidate Genes and Multi-Evidence Scores

| Symbol | Description | Direction | log2FC | padj | AS_event_count | AS_direction_major | AS_type_detail | Module | Evidence_score | Evidence_chain |
|---|---|---|---|---|---|---|---|---|---|---|
| Cryl1 | crystallin, lambda 1 | Downregulated | -1.978 | 3.348933669114433e-55 | 1 | down | A5SS:1 | redox and mitochondrial energy metabolism; lipid metabolism and xenobiotic detoxification | 71.125 | significant DEG evidence + AS event evidence + redox and mitochondrial energy metabolism; lipid metabolism and xenobiotic detoxification + candidate prioritization score |
| Npdc1 | neural proliferation, differentiation and control 1 | Upregulated | 3.708 | 3.610367147640154e-54 | 4 | down | IntronR:4 | Other | 70.468 | significant DEG evidence + AS event evidence + unclassified + candidate prioritization score |
| Tmem268 | transmembrane protein 268 | Upregulated | 3.26 | 4.623092048184446e-51 | 1 | up | A5SS:1 | Other | 59.548 | significant DEG evidence + AS event evidence + unclassified + candidate prioritization score |
| Idh3b | isocitrate dehydrogenase 3 (NAD + ) beta | Downregulated | -1.406 | 6.834416398594432e-49 | 1 | up | A5SS:1 | Redox / mitochondrial energy | 58.67 | significant DEG evidence + AS event evidence + redox and mitochondrial energy metabolism + candidate prioritization score |
| Mup2 | major urinary protein 2 | Downregulated | -6.625 | 2.476850371876817e-42 | 1 | down | 5pMXE:1 | Other | 57.55 | significant DEG evidence + AS event evidence + unclassified + candidate prioritization score |
| Decr2 | 2-4-dienoyl-Coenzyme A reductase 2, peroxisomal | Downregulated | -2.345 | 4.197822022434593e-39 | 1 | down | A3SS:1 | redox and mitochondrial energy metabolism; lipid metabolism and xenobiotic detoxification | 55.761 | significant DEG evidence + AS event evidence + redox and mitochondrial energy metabolism; lipid metabolism and xenobiotic detoxification + candidate prioritization score |
| Hectd2os | Hectd2, opposite strand | Downregulated | -3.794 | 9.006824772287428e-44 | 1 | down | IntronR:1 | Other | 53.328 | significant DEG evidence + AS event evidence + unclassified + candidate prioritization score |
| Cyp4f14 | cytochrome P450, family 4, subfamily f, polypeptide 14 | Downregulated | -2.569 | 7.369180316636613e-38 | 2 | up | IntronR:2 | Redox / mitochondrial energy | 52.37 | significant DEG evidence + AS event evidence + redox and mitochondrial energy metabolism + candidate prioritization score |
| Ces3a | carboxylesterase 3A | Downregulated | -3.518 | 2.529641846340484e-43 | 1 | up | 3pMXE:1 | Other | 52.326 | significant DEG evidence + AS event evidence + unclassified + candidate prioritization score |
| Dab1 | disabled 1 | Upregulated | 3.437 | 3.935921042876567e-43 | 1 | down | 3pMXE:1 | Other | 51.972 | significant DEG evidence + AS event evidence + unclassified + candidate prioritization score |

**Table A4** Prioritized AS-DEG Candidate Genes and Multi-Evidence Scores

| Symbol | Description | Direction | log2FC | padj | AS_event_count | AS_direction_major | AS_type_detail | Module | Evidence_score | Evidence_chain |
|---|---|---|---|---|---|---|---|---|---|---|
| Prr15l | proline rich 15-like | Upregulated | 3.961 | 1.20773936 99741e-41 | 1 | down | A3SS&ES:1 | Other | 51.533 | significant DEG evidence + AS event evidence + unclassified + candidate prioritization score |
| Fbxo6 | F-box protein 6 | Upregulated | 2.192 | 3.51682394 417081e-38 | 4 | down | A5SS:3; 5pMXE:1 | Other | 51.447 | significant DEG evidence + AS event evidence + unclassified + candidate prioritization score |
| Nit2 | nitrilase family, member 2 | Downregulated | -2.301 | 1.30150659 964173e-39 | 2 | down | IntronR:1; A3SS:1 | Other | 48.585 | significant DEG evidence + AS event evidence + unclassified + candidate prioritization score |
| Trmt2b | TRM2 tRNA methyltransfera se 2B | Downregulated | -1.367 | 4.08347107 312627e-41 | 1 | up | IntronR:1 | Other | 45.816 | significant DEG evidence + AS event evidence + unclassified + candidate prioritization score |
| Cd44 | CD44 antigen | Upregulated | 3.531 | 1.64248656 073067e-26 | 1 | up | cassetteExon:1 | inflammatory immunity and chemotaxis; cell adhesion, matrix remodeling and angiogenesis | 45.54 | significant DEG evidence + AS event evidence + inflammatory immunity and chemotaxis; cell adhesion, matrix remodeling and angiogenesis + candidate prioritization score |
| Syt1 | synaptotagmin I | Downregulated | -2.665 | 9.73347650 463199e-38 | 1 | down | A3SS:1 | Other | 45.035 | significant DEG evidence + AS event evidence + unclassified + candidate prioritization score |